JOURNAL OF PROPULSION AND POWER
Vol. 33, No. 2, March–April 2017

Investigation of Plasma Material Erosion Under Mechanical Stress

Aaron M. Schinder,* Julian J. Rimoli,† and Mitchell L. R. Walker‡
Georgia Institute of Technology, Atlanta, Georgia 30332

DOI: 10.2514/1.B36253

The operational lifetime of traditional Hall effect thrusters is limited by the erosion of the discharge channel walls. Erosion during long-duration life testing of Hall effect thrusters produces surface features that are unexplained by present models. Anomalous erosion ridges are one such unexplained feature. Hall effect thrusters are also expected to be under moderate (100 kPa to 6 MPa) thermomechanical stresses when operating, due to heat loads from the plasma. Thus, there may be a relationship between mechanical stress and the erosion features observed in Hall effect thrusters. This work investigates the plasma erosion of materials placed under mechanical loads. An experiment is designed to detect any changes to the erosion of material samples due to stress. Amorphous fused-silica samples are investigated in this paper. Fused silica erodes quickly and has no material heterogeneity. Three pairs of fused-silica samples, each pair with one control sample and one sample loaded to 6.0, 14.4, and 25.0 ± 1.1 MPa, respectively, are exposed to argon plasma for 11 h, producing erosion depths of 20–40 μm. Analysis of line scans made on the pre- and postexposure surfaces reveals the presence of a growth process operating on the initially roughened surface of the samples. Microscopy and line scans show the development of 100 μm parabolic cells bounded by sharp-edged cusps. No difference is detected in the development of surface features between unloaded samples and samples loaded up to 25.0 MPa. A model of the evolution of the surface accurately reproduces the development of the cell pattern, by taking into account the angle dependence of the atomic sputtering yield, yielding surfaces similar to those observed experimentally.

Nomenclature

B_i	=	angle dependence fitting coefficients, $1/\text{deg}^i$
E	=	Young's modulus, GPa
E_i	=	ion impact energy, eV
E_q	=	average energy of species q, J
E_{th}	=	sputtering yield threshold energy, eV
F	=	force applied to spring stack, N
$\hat{h}$	=	Fourier component of variational surface profile, m
I_{iw}	=	ion current to wall, A/m^2
K_g	=	nondimensional geometry-dependent field
k	=	scaling coefficient, mm^3/C
k_s	=	spring constant, N/m
$\frac{kT_e}{e}$	=	electron temperature, eV
L	=	length scale, m
m_i, m_e	=	ion and electron masses, kg
P	=	thruster discharge power, W
P_w	=	power flux to channel wall, W/m^2
Q_i, a, b, c	=	analytical fitting constants
T_r	=	temperature gradient in cylinder, K/m
T_{Thruster}	=	average thruster temperatures, K
T_0	=	average temperature, K
u	=	displacement, m
$Y(E, \theta)$	=	sputtering yield, mm^3/C
α	=	coefficient of linear thermal expansion, $\mu\text{m}/(\text{m} \cdot \text{K})$
σ_h	=	hoop stress, MPa
Γ_q	=	flux of species q to wall, $\text{particles}/(\text{m}^2 \cdot \text{s})$
ΔT	=	change in temperature from starting (293 K) temperature
ε	=	ion impact energy, eV
σ	=	stress, MPa
σ_b	=	standard deviation of slope of line fit
σ_r	=	radial stress, MPa
ϕ	=	sheath potential, V
Ψ	=	amplification function, nondimensional (ND)

Presented as Paper 2016-4842 at the 52nd AIAA/SAE/ASEE Joint Propulsion Conference, Salt Lake City, Utah, 25–27 July 2016; received 14 March 2016; revision received 5 July 2016; accepted for publication 7 July 2016; published online 8 September 2016.

*Graduate Fellow, Aerospace Engineering, 270 Ferst Drive. Senior Member AIAA.

†Goizueta Junior Faculty Professor, Aerospace Engineering, 270 Ferst Drive. Senior Member AIAA.

‡Associate Professor, Aerospace Engineering, 270 Ferst Drive. Associate Fellow AIAA.

I. Introduction

HALL effect thrusters (HETs) are a type of electrostatic thruster used to propel commercial, U.S. Department of Defense, and civilian spacecraft. HETs have been used for both station keeping and primary propulsion. HETs typically operate at specific impulses of 1300–3000 s, at efficiencies of 50% or more, and with 1–200 mN of thrust [1]. The operation of a HET and the main life-limiting processes are described in this section.

In a HET, neutral gas is injected by an anode gas distributor in the upstream end of an annular discharge channel. A cathode, which may be either external or center mounted, emits electrons. Some of the electrons neutralize the ion beam. Some of the electrons travel into the discharge channel, where they are trapped by a radial magnetic field. Crossed electric and magnetic fields generate a Hall current, which adds to the energy allowing the electrons to ionize the neutral gas. The electric field is established between the anode and a region of high electron density near the area of the maximum radial magnetic field. The electric field accelerates ions out of the HET to produce thrust. Some of the ions, due to either forming too close to the wall or due to the geometry of the electric fields, impact the wall downstream of where they form. Material is sputtered from the walls when the ion impact kinetic energy is greater than a certain sputtering threshold energy. Other failure mechanisms for HETs are possible, such as failure of the cathode or failure of the channel due to thermal shock. However, proper design can prevent these failure modes, and channel wall erosion is the primary life-limiting process [2].

Over time, atomic sputtering erodes the discharge channel wall and eventually exposes the magnetic circuit. This is considered the end of life for the HET, as continued operation of the HET will erode the magnet. This distorts the magnetic field, degrades performance, and ejects ferrous material into the spacecraft environment, which can cause electrical failures. Figure 1 shows aspects of the channel wall erosion process. Ions are formed in an ionization region and are accelerated in a thin (~10 mm) layer near the exit of the channel [3].

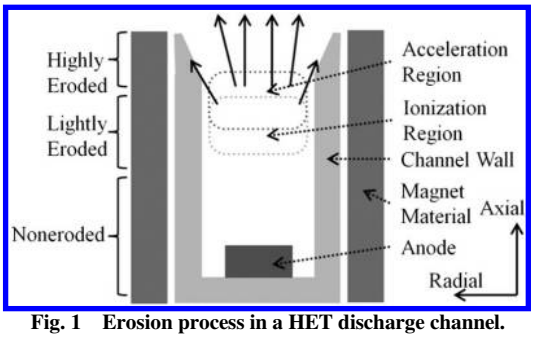

Fig. 1 Erosion process in a HET discharge channel.

Downstream of the acceleration region, where the ions attain enough kinetic energy to sputter material, the wall surface becomes microstructurally and macroscopically modified by the erosion.

Before being qualified to fly on a spacecraft, qualification life testing (QLT) is conducted to demonstrate 1.5 times the mission design life for all components of a HET, while using a particular set or sequence of operating voltages, gas flow rates, and field parameters. These tests are very expensive, requiring years of chamber time and a throughput of hundreds of kilograms of xenon.

Much work has already been done on the plasma erosion of materials in general and HET channel walls in particular. In sputtering yield experiments, ion beams are directed at material targets. Erosion of the material can be measured by several means, such as mass loss measurement, or by collecting sputtered material on a quartz-crystal microbalance (QCM) for angle resolved sputtered atom yields [4–6]. Garnier et al. [4,5] investigated the sputtering yield of boron nitride (BN), borosil (of a composition similar to M26), and aluminum nitride, with beams of xenon ions with incidence energies of 350, 500, and 1000 eV. They used weight-loss measurements to measure the sputtering yield. Yalin et al. [6] resolved the angular-dependent yield of sputtered material using a QCM. They measured yields for pure boron nitride, quartz, and kapton, at 100, 250, 350, and 500 eV, at 0, 15, 30, and 45 deg ion incidence angles.

Peterson et al. [7] conducted an empirical study of HET erosion using the NASA 120-M research HET. They inserted channel walls composed of grades A, AX05, and HP boron nitride and grades M and M26 borosil. After 200 h of exposure, they compared the rate of erosion, derived from depth measured with a laser profilometer, for the different materials.

Work has also been done to apply the aforementioned atomic sputtering yield models to model the evolution of a channel wall in HETs. HET plasma models use two-dimensional (2D) *r-z* axisymmetric models for the plasma, such as HPHall-2 [8] to obtain information about the ion density and ion impact rate. In this way, axisymmetric estimates for the channel wall geometry as a function of time can be made. Gamero-Castano and Katz [9] used HPHall to simulate the erosion of the channel wall of an SPT-100 HET. Hofer et al. [10] used HPHall-2 to reproduce the discharge channel wall erosion observed in the BPT-4000 qualification life test.

Despite being able to model average erosion profiles, there are still limitations to 2D axisymmetric erosion simulations using yield models that assume isotropic homogenous materials. Certain features that develop during long-duration life testing of HETs cannot be reproduced or explained by current models. One significant presently unexplained feature that appears during qualification life testing of HETs is the anomalous erosion ridges. These are azimuthal ridges, approximately 1 mm in wavelength, which are variations of the average erosion profile toward the exit plane of the HET. These ridges are observed during the QLT of several HETs, including the BPT-4000, SPT-100, and PPS-1350G [11–14]. Figure 2 shows the ridges that formed during the 10,400th h QLT of the BPT-4000.

Qualification life tests to date report only azimuthally averaged values for the channel wall erosion depth. Depth is reported as a function of axial position only. The existence of the anomalous erosion ridges has been reported, but the precise azimuthal position of the ridges has not been tracked during the erosion process, so it is unknown if they move in the azimuthal direction or are stationary.

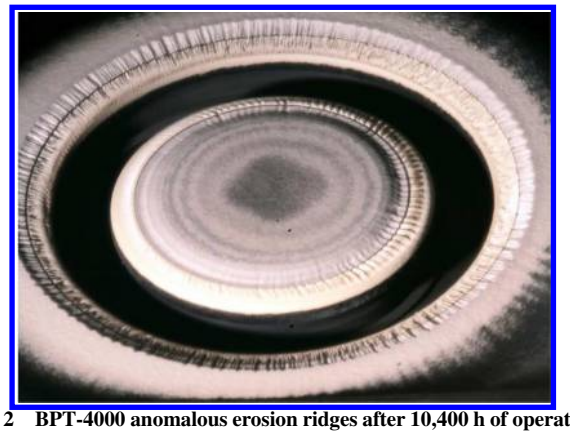

Fig. 2 BPT-4000 anomalous erosion ridges after 10,400 h of operation, reprinted with permission from Aerojet Rocketdyne.

De Grys et al. [15] state that the ridge depth adds 0.5 mm to the uncertainty of the erosion depth measurement of the BPT-4000. Researchers in the HET field have speculated that the anomalous erosion ridges are the result of electron dynamics. Morozov [14] notes the similarity between the electron cycloid length scale and the length scale of the anomalous erosion ridges during the Fakel Experimental Design Bureau 2000 h life testing of the SPT-100. In addition, Morozov et al. [16] proposed modeling the anomalous erosion ridges in terms of electron bombardment induced erosion in a paper on the modeling of electron dynamics in a HET. Mazouffre [17] investigated the anomalous erosion in the PPS-1350G and SPT-100 and stated that the spatial period of the erosion was on the order of the electron Larmor radius of around 1 mm and that the structure was more pronounced on the outer ceramic wall. In addition, he found that the grooves were slightly tilted in a direction opposite to the azimuthal electron drift.

Many other phenomena are present in the complicated physics in HETs. There are periodicities in the discharge current and ionization rate as well as other higher-frequency waves [3]. Common materials used in stationary plasma thruster (SPT) type HETs are boron nitride and borosil composites. Borosil composites have a complicated heterogeneous microstructure. Scanning electron microscopy (SEM) microscopy of M26 borosil revealed 10 μm flakes of BN suspended in a SiO_2 matrix, with up to 100-μm-wide regions of silica. Microstructural roughening similar to that observed in SEM microscopy of a HET channel wall are modeled to be the result of the material heterogeneity and differential sputtering rates of BN grains and SiO_2 [18]. In addition to these, other material-related processes could be affecting the process of plasma erosion.

One condition that could potentially influence the erosion process of the discharge channel wall is the thermomechanical stress present in the material while the HET is in operation. Theoretical and experimental work demonstrates the importance of mechanical stress in the evolution of surfaces in stress corrosion cracking. Suo [19] gives variational laws for the evolution of surfaces based on the maximum reduction in free energy. Suo states that thin films with mismatches between the crystal substrate lattice constant and the film lattice constant experience high stresses and have been known to evolve into strands and islands through mass diffusion during corrosion. Asaro and Tiller [20] investigated the initiation of cracks in materials with surface distortions using a perturbation analysis. They found a criterion for wave amplitude growth as a function of wave number and stress in the presence of tensile or compressive stresses. Kim et al. [21] found a similar criterion for the evolution of surfaces, relating the square of the stress state to a wave number scale for the amplification of surface features. They measured the growth of wave modes in an aluminum surface placed under plastic deformation when etched with nitric acid. Because stress has proven to be important in other erosion processes, it is thought that stress might play a role in plasma erosion in HETs.

During operation, HETs experience significant thermal loads, potentially leading to high thermomechanical stresses. During the operation of a HET, the energetic plasma in the thruster interacts with

the walls of the channel. Mediated by the plasma sheath, fluxes of ions and electrons provide a heat flux to the wall [3,25]. This heat flux into the wall is balanced by thermal radiation from the inner surfaces of the channel wall, which cool the thruster, and by (limited, by design) conduction to the thruster body.

Modeling is conducted to obtain estimates for representative thermomechanical stresses that are present in HET channel walls during operation. This modeling is informed by prior experimental measurements of HET channel wall temperatures. Mazouffre et al. [22] investigated the SPT100-ML and the PPSX000 using a mid-wave infrared (MWIR) (8–9 μm spectral domain) thermal infrared camera. The average temperatures of the BN–SiO_2 channel walls were well characterized by a power-law relationship, given in Eqs. (1) and (2). The discharge power, in W, is given by P. The thruster channel wall temperature is given by T. The ranges for these relationships are 500–3000 W for the SPT-100 and 1500–5000 W for the PPSX000. Temperatures as high as 900 K are attained during 5 kW operation of the PPSX000,

$$T_{\text{SPT100}} = 447\ \text{K} + (11.1\ \text{K/W}^{0.5})P^{0.5} \tag{1}$$

$$T_{\text{PPSX000}} = 429\ \text{K} + (6.8\ \text{K/W}^{0.5})P^{0.5} \tag{2}$$

Data and infrared images were presented for a 3.2 kW operating condition, showing a ~6–10 K difference between the top and bottom of the outside channel wall and a 60 K difference between the inside and outside channel wall.

Martinez et al. [23] investigated the T-140 HET thermal behavior by placing thermocouples within holes drilled into the channel wall, 1 mm from the plasma facing surface, and in certain other locations around the thruster. The T-140 has an approximately 140 mm outer diameter channel, which is composed of grade M26 boron nitride. Temperature measurements were made at several discharge powers, and a similar power-law relationship between maximum channel wall temperature and discharge power was derived. This relationship is shown in Eq. (3):

$$T_{\text{T140}} = 302\ \text{K} + (24\ \text{K/W}^{0.38})P^{0.38} \tag{3}$$

In the paper of Martinez et al. [23], temperature distributions over the channel were presented for the 840 W, 5.1 mg/s run condition. Temperatures were approximately 610 K at the exit plane of the channel and 574 K near the inlet of the channel.

Dimensional analysis of thermomechanical problems and analysis of one-dimensional analytical thermomechanical models for cylinders provide some generally applicable scaling relationships between important quantities. One such scaling law for the stress is given in Eq. (4). In this expression, the stress at a given point σ scales with a nondimensional constant K_g, the material properties, and the temperature difference across the geometry, or a length scale and temperature gradient. This dimensional analysis assumes linear elasticity of the object in question and a constant coefficient of thermal expansion (CTE). These conditions hold for ceramic materials (small deformations) and typical HET temperature ranges. K_g is a function of the nondimensional problem geometry and Poisson's ratio. The relevant material properties are the Young's modulus E and CTE α. Equation (4) tells us that, because of material property differences, we should expect a greater thermal stress, by a factor of 10, in channel walls composed of borosil (M, M26) when compared to HP boron nitride,

$$\sigma = K_g E\alpha\nabla(\Delta T)L = K_g E\alpha(T_2 - T_1) \tag{4}$$

A 2D axisymmetric thermomechanical model was created for the T-140 channel wall. The T-140 channel wall is surrounded by a titanium radiation shield on the inner face and by a titanium radiation shield bucket on the outside that loosely supports the inner shield. The channel wall is held to the bucket by rivets along the bottom of the channel and by tension from the stem holding the bottom of the anode-gas distributor to the bottom of the channel. Thermally insulated boundary conditions are justifiable for the titanium radiation shield, which is in loose thermal contact with the channel, but not very thermally emissive. Thermal emissivity of unfinished titanium is given as 0.31 in [31]. A value of 0.241 is given by [32]. A thermal insulating gap is present between the upper channel wall and the surrounding magnet material on the inside of the inner wall and outside of the outer wall. Radiative boundary conditions are applied to the inside faces of the thruster. The joint between the channel wall and the thruster implies loose mechanical boundary conditions.

Heat flux to the channel wall is a function of the local plasma density and the electron temperature. This can be derived from the physics of the plasma sheath for a dielectric discharge channel wall. Positive and negative charge fluxes to a dielectric wall must balance, and so a region of negative potential forms near the wall to repel the lighter and more mobile electrons. The power density to the channel wall can be expressed in terms of the fluxes of electrons and ions to the channel wall times the energy that each carries, given in Eq. (5). Secondary electrons are ejected from the wall with a low energy (1–2 eV), so their direct contribution to the power flux to the wall can be neglected [3]. Secondary electrons have a more significant effect on heat flux to the wall due to their effect on sheath potentials [3],

$$P_w = \Gamma_e E_e + \Gamma_i E_{\text{total}.i} \tag{5}$$

This can be reexpressed [Eq. (6)] in terms of the ion current to the wall, in a form given in Goebel and Katz's analysis in ([3] Chap. 7). In the following equations, P_w refers to the heat flux to the channel wall, I_{iw} refers to the ion current density to the wall (unit charge times bohm velocity times plasma density), ε refers to the ion energy (in this case due to the Bohm velocity), ϕ refers to the plasma sheath potential, m_i refers to the ion mass, m_e refers to the electron mass, and T_e refers to the electron temperature,

$$P_w = I_{\text{iw}}\left[e^{\frac{e\phi}{kT_e}}\sqrt{\frac{2m_i}{\pi m_e}}\left(\frac{kT_e}{e}\right) + (\varepsilon - \phi)\right] \tag{6}$$

Secondary electron emission (SEE) is the emission of electrons from a material stimulated by electron bombardment of the material at a given energy. SEE tends to reduce the magnitude of the plasma sheath potential drop, which leads to greater heat fluxes to the channel walls [3]. Hobbes and Wesson state that for a SEE space-charge limited sheath (one with the maximum amount of SEE possible from the wall) the sheath potential is limited to $1.02kT_e/e$, where kT_e/e is the energy due to the electron temperature divided by the charge in volts [25]. For a standard Child–Langmuir sheath, the sheath potential is $-5.96kT_e/e$ for xenon. For a borosil wall, assuming the SEE model for borosil given by Goebel and Katz, sufficient SEE for the space-charge limited case is present for electron temperatures greater than 30 eV [3]. For 25 eV, the sheath potential is roughly −54 V [3]. For several values of the electron temperature, Eq. (6) reduces to Eq. (7), with the first term in square brackets being the energy flux to the wall due to electrons and the second being due to ions,

$$\begin{cases} P_w = I_{iw}\left(\frac{kT_e}{e}\right)[1 + 6.47], & T_e < 10\ \text{eV, Xe, BNSiO}_2 \\ P_w = I_{iw}\left(\frac{kT_e}{e}\right)[45.02 + 2.61], & T_e = 25\ \text{eV, Xe, BNSiO}_2 \\ P_w = I_{iw}\left(\frac{kT_e}{e}\right)[140.76 + 1.52], & T_e > 30\ \text{eV, Xe, BNSiO}_2 \end{cases} \tag{7}$$

These equations show that the most significant heat flux to the wall will occur in the ionization and acceleration regions of the HET, where the plasma density and electron temperatures are high. For typical ion densities of 1×10^{17} particles/m^3, at electron temperatures of approximately 25 eV, heat fluxes on the order of 8 W/cm^2 are expected. Conditions similar to these are present in multikilowatt HETs. Martinez [23] calculates a peak heat flux of 10 W/cm^2 for a 2.7 kW operating condition for the T-140 thruster, based on experimental temperature measurements. Katz et al. [24] calculate that for a baseline, unshielded configuration of a 12.5 kW thruster, peak heat fluxes of 10–15 W/cm^2 are expected [24].

Under varying operating conditions, the heat flux lost to the wall as a percentage of the total discharge power has been found to remain relatively constant [22,23]. For the T-140, average and peak temperatures similar to those reported by Martinez [23] are found if ~25–27% of the discharge power is applied as a heat flux to the ionization/acceleration region of the T-140 thruster channel wall. In comparison, Goebel calculates a 32% discharge power loss to the wall for an SPT-100, given assumptions of 25 eV electron temperatures [3]. This proportion (25–27%) of the discharge power reproduces Martinez's average temperature curve in both the 2D modeling and a simple bulk radiative heat balance model [22]. Figure 3 shows the T-140 channel, the surrounding structures, and the boundary conditions used in modeling the channel wall. Figure 4 shows the temperature and hoop stresses for the 840 W operating condition of the T-140, which can be compared to Fig. 5 from [22].

Table 1 presents the different operating conditions and variations on the material and boundary conditions. Material properties used in the simulation are taken from the St. Gobain boron nitride solids material data sheet [26]. An emissivity of 0.9 was used for the M26, similar to the value used in [23]. To make a conservative estimate for stresses, the maximum Young modulus and minimum thermal conductivity were used. A Young modulus of 94 GPa, a CTE of 1.5 μm/m · K, and a thermal conductivity of 11 W/(m · K) were used for borosil. A Young modulus of 40 GPa, a CTE of 0.6 μm/(m · K), and a thermal conductivity of 27 W/(m · K) were used for grade HP boron nitride. The expected reduction in stress for using grade HP as a wall material is present. Representative

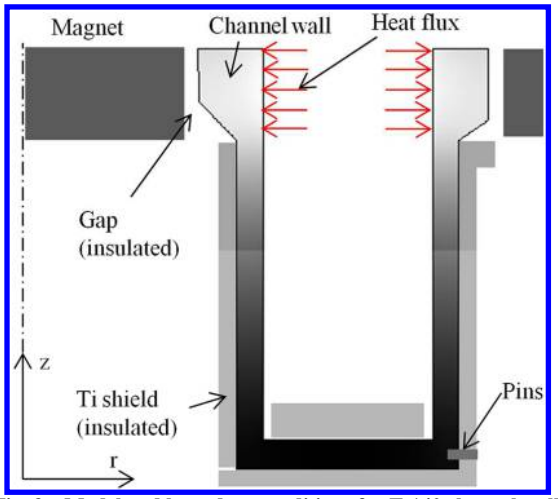

Fig. 3 Model and boundary conditions for T-140 channel wall.

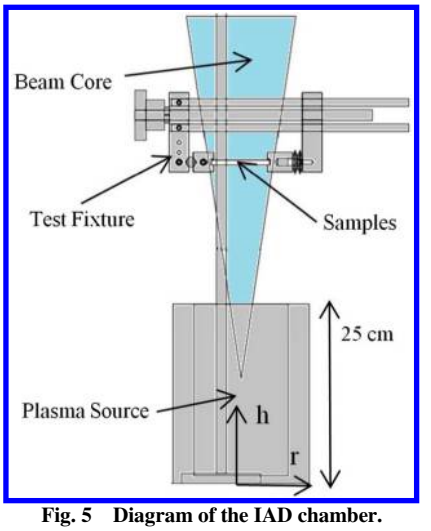

Fig. 5 Diagram of the IAD chamber.

thermomechanical stresses for the T-140 are in the 100 kPa to 6 MPa range, according to this modeling. The maximum stress that M26-, M-, and HP-grade BN can withstand is in the range of 20–30 MPa. This is the flexural strength of the material [26]. Any stresses greater than this will crack the channel wall.

The work given previously provides a range of representative thermomechanical stresses. Using these, it is desired that the effects of this thermomechanical stress on the atomic sputtering erosion behavior of materials be explored. An experiment is designed with the goal of observing any alteration to the process of plasma erosion of a material due to the application of mechanical stresses and mechanical strain energy.

II. Design of Experiment

An experiment is designed to detect and characterize features amplified by a plasma erosion process. The experiment is specifically designed to look for changes to plasma erosion due to the presence of mechanical stress and elastic strain energy. The stress range for the experiment (6.0–25.0 MPa) is chosen to be at least as large as the largest anticipated stresses in HET channel walls (6 MPa), up to the maximum load that can be reliably applied to the tested material without cracking. It is proposed that any modification to the erosion of a material due to thermomechanical stress will be more pronounced with greater stress and that the largest possible stress present in any engineering scenario is necessarily less than that which causes fracture. The experiment is divided into three phases: a preexposure

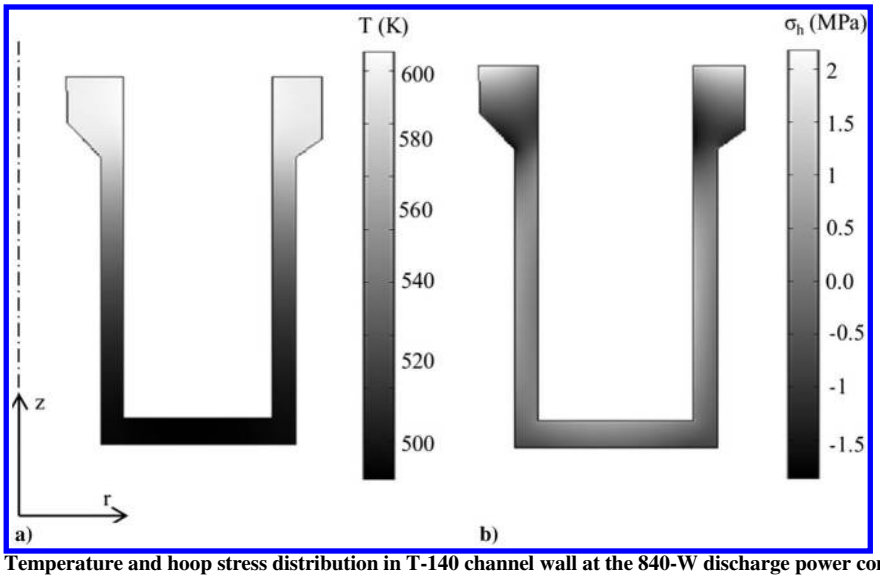

Fig. 4 Temperature and hoop stress distribution in T-140 channel wall at the 840-W discharge power condition.

Table 1 HET thermal modeling summary

Wall material (grade)	Discharge power, W	Outer thermal boundary condition (BC)	Max temperature, K	Max compressive hoop stress, MPa
M26	840	Insulated	605	−1.89
M26	2000	Insulated	779	−3.82
M26	2800	Insulated	862	−4.93
M26	3400	Insulated	913	−5.69
HP	840	Insulated	576	−0.15
HP	3400	Insulated	808	−0.44
M26	840	Radiating	564	−2.06
M26	840	Radiating	873	−6.14
HP	840	Insulated	576	−0.15
HP	1500	Insulated	674	−0.26
HP	2000	Insulated	732	−0.33
HP	2400	Insulated	807	−0.44
HP	3400	Insulated	855	−0.52

phase, a exposure phase, and a postexposure phase. In the preexposure phase of the experiment, material samples are profiled using a Tencor P-15 contact profilometer and imaged using an Olympus LEXT confocal microscope (LEXT). In the exposure phase, material samples are placed under a mechanical load and eroded with a plasma source. In the postexposure phase, the samples are profiled again and imaged with the LEXT. The pre- and postexposure profiles are compared to derive the amplification function Ψ, which provides information about which features (as a function of wavelength/wave number) are growing and which are being damped.

A. Chamber Characterization

All work for the erosion phase is performed in the Georgia Tech Research Institute Ion-Assisted Deposition (IAD) chamber. The IAD chamber contains a plasma source capable of supplying an argon plasma discharge at discharge voltages of up to 120 V. The ion current density and ion energy distribution function (IEDF) of the plasma was characterized with Faraday probe and retarding potential analyzer (RPA) measurements. The Faraday probes used for the characterization were 0.865 in outer diameter (OD) circular planar probes surrounded by a 0.938 in inner diameter (ID) cylindrical shield, similar to the Jet Propulsion Laboratory (JPL) Faraday probes in [33]. The RPA is a four-grid RPA with floating, e-repulsion, ion-repulsion, and e-suppression grids in front of a circular collector [34]. These measurements were conducted at heights of 40 and 60 cm from the floor of the chamber and at several different axial locations. Table 2 presents the plasma source operating conditions for which the source was characterized. Figure 5 shows the test fixture positioned over the source in the IAD chamber. Figure 6 shows the ion current densities vs the distance from the source axis for three 40 cm characterizations. For Fig. 6a, several Faraday probe sweeps were taken, and the results were averaged. The standard deviation of the sweeps is roughly 0.04 $\mathrm{mA/cm^2}$, which is too small to be seen in the figure. RPA measurements of the IEDF for a 140 V bias voltage condition show a distribution of primary ions with a center energy of 130 eV and a standard deviation of 20 eV. Figure 6b shows the IEDF. During the experiment exposures, a bias voltage of 120 V is used to ensure stable long-term operation of the plasma source. The ion current density profile for Condition B shows an axial ion current density of 2.5 $\mathrm{mA/cm^2}$ and a falloff of 2/3 at a radius of 4 cm from the plasma source axis.

Table 2 Plasma source operating conditions for characterization

	Condition A	Condition B	Condition C
Coil current, A	2.03	2.03	2.08
Argon flow, sccm	10	10	12
Discharge current, A	49	50	49.5
Bias voltage, V	140	120	140
Discharge voltage, V	119	— —	120
Discharge power, kW	5.86	— —	5.79

B. Material Selection

Fused silica is chosen as the sample material for the experiment, with Technical Glass Products supplying the fused-silica samples. Fused silica is amorphous and isotropic; it has a disordered noncrystalline structure without grain boundaries or other microstructural detail. BN and borosil composites (BN–SiO_2) are common materials used in HETs. These materials differ from the simple material chosen for the test in several ways. Previous SEM images of cross-sections taken from M26 borosil show a complicated microstructure with 0.1×100 μm h-BN flakes suspended in a silica matrix, with scattered silica voids as large as 100 μm on a side [18]. Other BN ceramics are also formed by hot pressing a powder and probably also have significant heterogeneities in their microstructure. It is known from the work of Garnier et al. [4,5], as well as from previous work investigating and simulating the erosion of heterogeneous BN–SiO_2 [18], that plasma erosion of these materials forms surface features driven by heterogeneities in the material. Differences in the sputtering yield of each component lead to the protrusion of the lower sputtering sputtering-yield BN, which shields the silica behind it, leading to structures that Morozov [14] calls "pike-tongue" structures. In the paper [18], they are referred to as "cliff and valley" structures. These structures are oriented normal to the ion flow direction, as opposed to along it, and do not seem to correspond to or develop into the phenomena responsible for the anomalous erosion ridges.

The goal of this experiment is to detect whether or not the presence of mechanical stress, hypothetically through variations in the surface profile leading to variations in strain energy density and changes in local yield, leads to changes in the way certain surface features grow. The plasma source is only capable of operating for 12 h at a time in a uniform manner, so the total erosion depths that can be developed on the material samples are limited. Depths of 10–40 μm for fused silica are estimated using yield models and the characterization of the plasma. Fused silica is a fast eroding material that will allow the effects of mechanical stress, or instabilities driven by mechanical strain energy, if any, to be isolated from any effects due to the microstructure. Because of this, fused silica is chosen as the sample material for this paper, to attempt to detect whether these effects exist in a simple situation. It is expected, based on previous work [18], that the erosion of borosil and boron nitride under stress will have a significantly different character, dominated by the material microstructure and difficult to model analytically.

Technical Glass Products lists a Young modulus for their material of 72 GPa [27]. A compression test was performed on the samples to obtain an accurate and independent experimental value for the Young modulus. Several $1 \times 1 \times 0.25$ in fused-silica samples were instrumented with WK-02-062AP/W strain gages from Vishay Micro Measurements, with a strain accuracy of ± 0.1 $\mu\varepsilon$. The strain gages were used to measure axial strain from the center of the sample face. The samples were placed in a compression frame in an Instron 5900 material testing device. The Instron measured the applied load. The samples were compressively loaded from 0 to 500 lbf, and an experimental value of 58.7 ± 2.4 GPa was obtained for the material. This value is used to convert the measured strain into a stress/load state during the experiment.

Samples with dimensions $3 \times 1 \times 0.25$ in. were used in the stressed erosion experiment. This size was used so that a sufficiently large (>3 cm) region of the samples had a uniform uniaxial stress, away from edge effects of the grips applying the load. The sample size was bounded above by the need to avoid bending stresses and the need to fit within the beam core of the plasma source.

C. Test Fixture Design

A test fixture is designed to apply, in a moment-free manner, an even (95% uniaxial) compressive load to material samples. The test fixture is designed to meet several requirements. It must maintain an even compressive load on a rigid and brittle material, in a vacuum

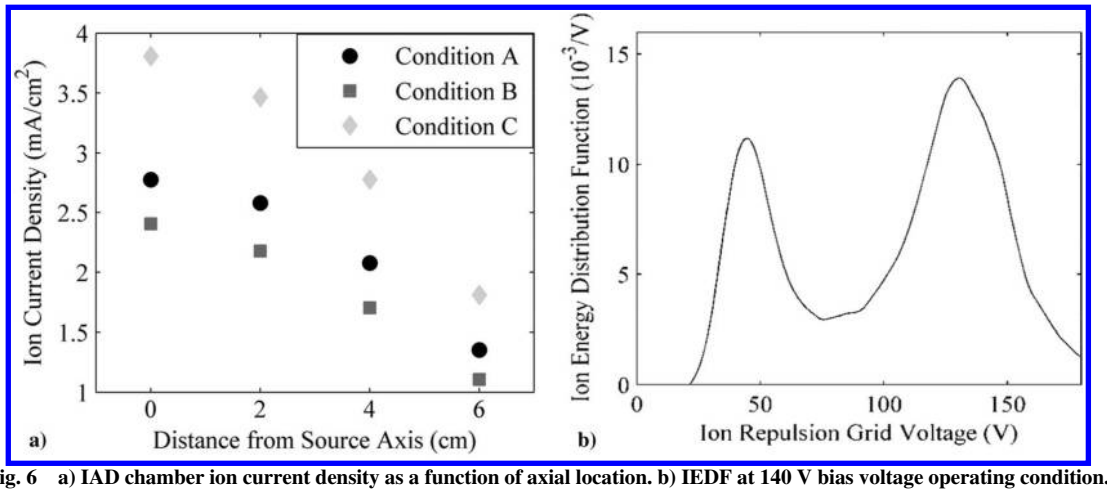

Fig. 6 a) IAD chamber ion current density as a function of axial location. b) IEDF at 140 V bias voltage operating condition.

chamber. It must apply the compressive load without bending moments. It must maintain the load while being heated by exposure to the plasma, with the fixture reaching temperatures as high as 250°C.

The test fixture grips are made of 304 stainless steel. A medium carbon steel 1/2"-20 threaded rod tightens the grips, while medium carbon steel guide rods keep the grips aligned. A ball bearing joint on the left grip ensures that compression will be applied to the sample in a moment-free manner. Cushions of PTFE tape are applied to the left and right grips to provide a conforming layer between the grips and sample for even loading. The right grip is a plunger that sits on a stack of Belleville springs, or conical disc springs. The springs are intended to maintain the applied mechanical load as the sample and test fixture heat up and thermally expand. The springs apply a load over a much longer travel distance than the thermal expansion (they have less effective rigidity than all other members of the system), and so minor changes in length due to thermal expansion only lead to small reductions in the load applied by the springs. This relaxation is characterized and quantified by the experiments in the next section.

The test fixture is designed to hold two samples beside each other over the plasma source. The grips hold the loaded experiment sample. A sheet metal basket holds an unloaded control sample next to the experiment sample. A thermocouple is attached to the top of the plunger, allowing temperature measurements to be made of the test fixture. A preheater circuit made of two nichrome wire grilles, insulated by Aremco Ceramabond 571-P, is attached to the top and sides of each grip. The preheater circuit is available to warm up the clamp and sample to equilibrium temperatures before exposing the sample to the plasma. Figure 7 shows a diagram of the test fixture. Figure 8 shows the test fixture and peripheral attachments set up in the IAD chamber.

D. Characterization of Thermal Relaxation of Applied Load

An initial load was applied to each loaded sample by the test fixture, before closing the chamber and exposing the sample pair. This load relaxed as the test fixture heated up to an equilibrium temperature of approximately 220–250°C. The screw and metal parts

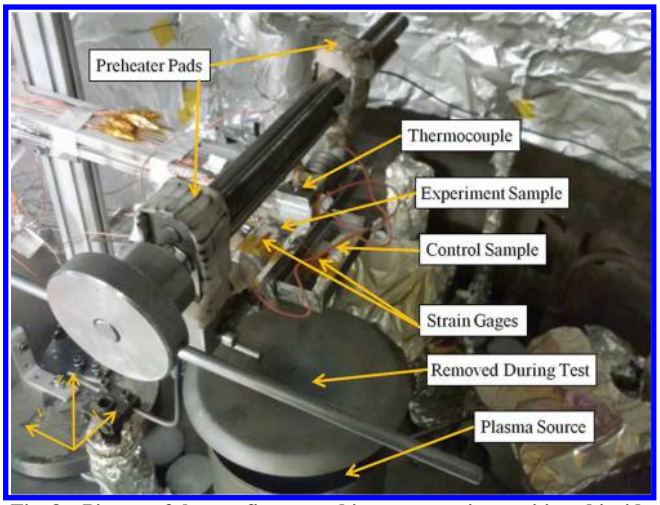

Fig. 8 Picture of the test fixture and instrumentation positioned inside the IAD.

of the clamp thermally expanded more than the material sample, leading to a net extension of the spring stack. The spring constant of the spring stack was designed to be compliant enough that thermal relaxation is acceptable, while still stiff enough to have a linear range that spans the loads of interest for the experiment.

Direct measurement of the relaxation of the fixture during preheating and exposure to the plasma was attempted using the strain gages attached to the samples. Even when the strain gages were successfully insulated from the plasma with silicone RTV, the temperature sensitivity of the gages (as high as 6 $\mu\varepsilon/°C$) was difficult to correct for. In addition, the internal junctions in the strain gages melted at 220°C, placing an upper bound on the temperature at which the fixture relaxation could be measured. Extrapolation was needed to extend measurements to the equilibrium fixture temperatures obtained during testing.

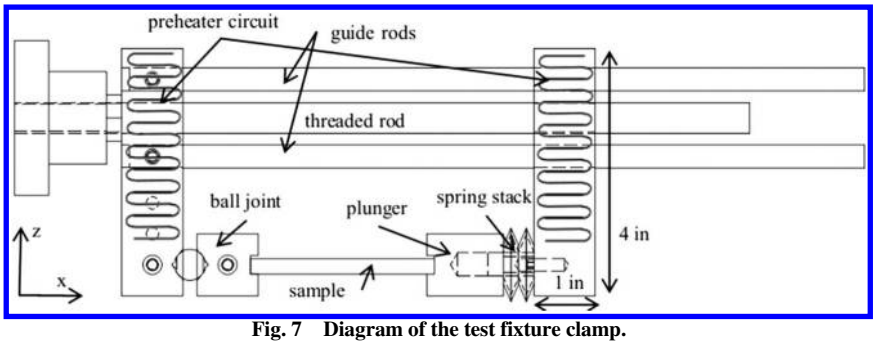

Fig. 7 Diagram of the test fixture clamp.

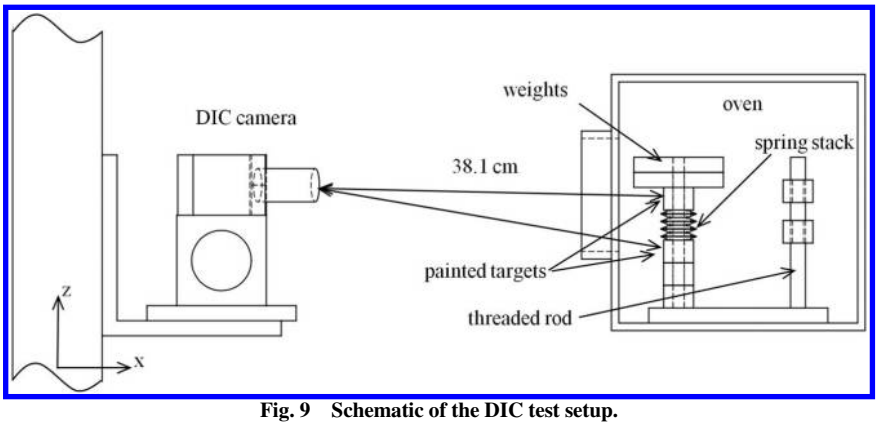

Fig. 9 Schematic of the DIC test setup.

Direct and indirect measurement of the clamp relaxation were made ex situ using a Sun Systems EC1A environment chamber and an Aramis 5M digital image correlation (DIC) system. The DIC system consists of two cameras at a fixed angle on a moveable mount. Only one camera was used for this experiment. The camera observed the deflection and deformation of motion targets, which were painted with a high-temperature speckle pattern. Four measurement series were made with the DIC/oven system, shown in Fig. 9.

The first measurement observed the thermal expansion of the threaded rod used in the clamp. Two painted targets were placed with a distance of 15.0 mm from the bottom edge of the upper target to the top edge of the lower target. The camera was placed at a horizontal distance of 38 cm from the target rod, and both motion targets were in the field of view. The deflection statistics of an approximately 2-mm-wide region of the top and bottom motion targets were collected. The difference between the vertical deflections was taken to be the extension of the 15.0 mm region of the threaded rod. Deflections at eight temperature set points between 20 and 280°C were measured. Temperatures in the oven were allowed to equilibrate upon reaching each set point for 20 min. The uncertainty bound for the thermal expansion coefficient was found using the expression for the uncertainty of the slope given in Eq. (8), corresponding to one standard deviation. The thermal expansion of the threaded rod was measured to be 8.24 ± 0.35 μm/m-°C. In Eq. (8), σ_b is the uncertainty of the slope, $\hat{y}_i$ is the linear regression to the data at each x_i, and N is the number of data points:

$$\sigma_b = \sqrt{\frac{\sum (y_i - \hat{y}_i)^2}{(N-2)\sum (x_i - \bar{x})^2}} \tag{8}$$

The purpose of the second set of measurements was to measure the relative change in stiffness of the spring stack as a function of temperature. In these measurements, a series of light disc springs made of the same material, by the same manufacturer as the springs used in the test fixture, were loaded with weights. Temperature ramps were conducted to measure the extension vs temperature of the light spring stack, $u(T)$. The light spring stack allowed the DIC system to resolve larger displacements and provided reasonable uncertainty bounds for the relative stiffness $k(T)/k_0$. Because the springs used in the test fixture were very stiff (1540–1600 N/mm), weights were insufficient to provide resolvable differences in extension.

A one-dimensional version of the elastic deformation equations with thermal expansion is given in Eq. (9),

$$(u - \alpha L \Delta T) = \frac{F}{k(T)} \tag{9}$$

The net displacement of the spring is given by u. The load provided by the weight stack is given by F. The CTE is α. The spring constant as a function of temperature is $k(T)$. Subtracting the extension values at two different load levels removes the change in extension due to thermal expansion (assuming small deflections relative to the initial height). This leaves only a change in relative extension due to the change in the spring constant at each temperature. This is shown in Eq. (10),

$$k(T) = \frac{F_2 - F_1}{u_2(T) - u_1(T)} \tag{10}$$

The relative spring constant stiffness, as a function of temperature, is given by Eq. (11). A linear model is appropriate over the temperature range of interest. Good agreement exists between k/k_0 and E/E_0, the change in elastic modulus for austenitic stainless steels provided by American Iron and Steel Institute (AISI) [28]. The springs lose 8% of their stiffness at a temperature of 250°C

$$k(T) = k_0\left[1 - \left(2.714 \pm 0.382 * 10^{-4}\frac{1}{C}\right)\Delta T\right] \tag{11}$$

Direct measurements of the room temperature spring constant of the fixture spring stack were made using an Instron 5982 material testing system. Two stacks of eight Belleville-disc springs were placed between 1 in. × 1 in aluminum beams in the apparatus shown in Fig. 10. The aluminum beams were pressed by the Instron compression grips.

Extension was measured for loads from 0 to 9677 N. The springs behaved linearly, after about 1 mm (2413 N per spring stack) of compression. Three load ramps were conducted, measuring an average spring constant of 1597 ± 2 N/mm for each stack. This corresponds well with an earlier measurement made using the test fixture screw to measure spring displacement and the strain gage on the sample to measure load made in situ on the test fixture (1540 ± 63 N/mm).

Using these ex situ measurements, the relaxed load of the test fixture can be calculated as a function of the initial load and the temperature measured on the test fixture. This calculation takes into account thermal expansion, changes in spring constant, and variability in the clamp behavior. Equation 12 shows the calculation for the relaxed load. The force applied by the test fixture is given by F. The temperature is T, and a change in temperature from room

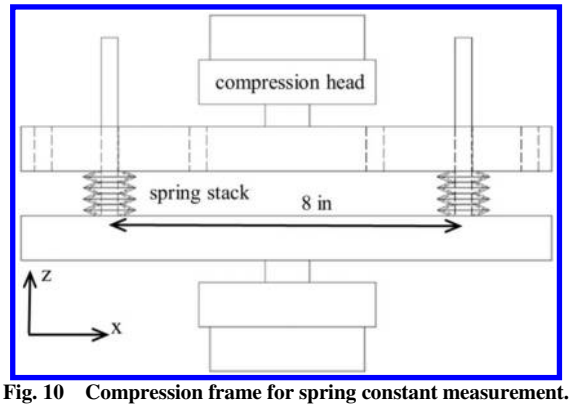

Fig. 10 Compression frame for spring constant measurement.

temperature is ΔT. The initial spring compression is u_0. The length and CTE of the threaded rod are L_{rod} and α_{rod}. Observed variability in the clamp behavior is u_{var}.

Table 3 presents the values for the constants. Table 4 presents the values calculated for the relaxed load,

$$F(T, u_0) = (k_0)(1 - k_s \Delta T)(u_0 - \alpha_{\text{rod}} L_{\text{rod}} \Delta T \pm u_{\text{var}}) \tag{12}$$

E. Stressed Erosion Test Procedure and Analysis

The test is conducted in three phases: a preexposure phase, an exposure phase, and a postexposure phase. In the preexposure phase, each of the samples exposed to the plasma is instrumented with a WK-02-062AP/W strain gage from Vishay Micro Measurements. Each of the preroughened samples is roughened with 320-grit, then 500-grit SiC powder and a glass cover plate until an even pattern of surface roughness is formed. Each sample is scanned in the Tencor P-15 profilometer. A series of line scans is taken at 50 different y locations, beginning along the centerline of the sample, and offset in x by 20 μm to provide representative roughness statistics for the initial surface. The Tencor profilometer has a vertical resolution accurate to within 0.5 A and a vertical range of 327 μm. Roughness statistics are compiled from the center 36.6 mm so that edge effects may be avoided. An Olympus LEXT 3D confocal microscope is used to collect visible and laser images and height maps from three locations on each sample. These locations are returned to posttest to compare pre- and posttest surface profiles and features. Figure 11 shows certain regions on the exposed sample. The area away from the boundary conditions, used to derive ψ, is indicated by the shaded box.

In the exposure phase of the experiment, pairs of samples were placed in the test fixture, located 6 cm above the plasma source can. One of each sample pair was placed in the clamp grips (the loaded sample), and one was placed in the basket to the side of the test fixture (the control sample). The thermocouple and strain gage instrumentation was connected. The clamp was tightened until a strain corresponding to the desired initial load was achieved. The chamber door was closed, and the chamber was pumped down. Then, the preheater circuit on the test fixture was activated, and the test fixture is heated to approximately 100°C. Next, the preheater is turned off, and the plasma source was turned on. The samples were exposed for 11–12 h. Finally, the chamber was vented, and the exposed samples were removed from the fixture.

In the postexposure phase, new line scans were conducted with the Tencor P-15 contact profilometer. The amplification function was derived from the Fourier transform of the pre- and posttest line scans. The erosion depth was also found from the step height at the corners of the samples. Posttest microscopy was conducted with the Olympus LEXT microscope. The same locations, measured from the lower left-hand corner of the samples with the motion stage (accuracy of approximately 10 μm), were revisited to provide microscopy comparisons.

Table 3 Relaxation calculation variables

Variable	Value
k_0, N/mm	1597 ± 2
k_s, 1/°C	$2.714 \pm 0.382 \times 10^{-4}$
α_{rod}, μm/(m · °C)	8.24 ± 0.35
L_{rod}, mm	165.1
u_{var}, mm	0.07

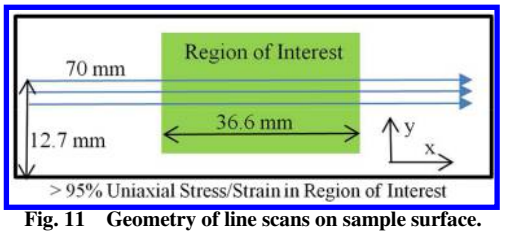

Fig. 11 Geometry of line scans on sample surface.

The pre- and posttest profilometry data are analyzed in order to derive an amplification function, denoted by Ψ. The amplification function is a nondimensional measure of which Fourier wave modes are being amplified by the erosion process and which are being damped. Ψ is defined in Eq. (13). Each line scan provides a height profile $h(x)$, which can be Fourier transformed. A pair of pre- and post-test line scans yields an amplification function,

$$\Psi = \log_{10}\left(\frac{\hat{h}_t(\omega)}{\hat{h}_0(\omega)}\right) \tag{13}$$

Uncertainty in the amplification function can be estimated from the spread in the amplitude of each wave mode by differentiating. Equation (14) shows this relationship. Because the amplification function is a relative measure, the uncertainty is proportional to the spreads in amplitudes divided by the amplitudes. Data from the Tencor P-15 have a noise floor of 0.05 μm. Initial and final surface amplitudes are approximately the same order: 0.01 to 0.001 μm for all but the smallest wave modes, with standard deviations of approximately half the magnitude. The standard deviation of the mean is the deviation of $\hat{h}$ divided by the square root of the number of line scans. Because of this, uncertainties as high as ± 0.15 for Ψ are present in the measurements,

$$\Psi(\omega; t) \pm \Delta\Psi = \log_{10}\left(\left|\frac{\hat{h}_t(\omega)}{\hat{h}_0(\omega)}\right|\right) \pm \left(\left|\frac{\Delta h_t}{h_t}\right| + \left|\frac{\Delta h_0}{h_0}\right|\right) \tag{14}$$

III. Results

Four exposures were conducted. Three of the exposures were with preroughened samples, with a series of increasing loads applied to the loaded sample. One exposure was with smooth (as manufactured) samples, with surface variations of less than ± 0.05 μm, as measured by the Tencor profilometer. Table 4 shows a summary of the exposures. The loaded and control sample numbers are given so that data may be computed with the conditions of each exposure. The equilibrium temperature was the fixture temperature at which the majority of the exposure (after approximately 30 min of warmup time) took places, measured by the type-K thermocouple on the fixture. The relaxed stress state was the stress in the sample, calculated by Eq. (12) for the given equilibrium temperature and the

Table 4 Exposure overview for increasing stress series, for fused-silica samples

Exposure	Exp. 1	Exp. 2	Exp. 3	Exp. 4
Loaded sample	SA7	SA1	SA8	SA6
Control sample	SA4	SA5	SA9	SA10
Initial stress state, MPa	9.6	17.5	18.1	29.1
Equilibrium temperature, °C	288 ± 12	225 ± 8	224 ± 5	243 ± 5
Relaxed stress state, MPa	6.00 ± 1.01	14.36 ± 1.01	14.94 ± 0.97	24.99 ± 1.10
Relaxed stress state, % orig	62.5 ± 10.5	82.05 ± 5.79	82.57 ± 5.36	85.87 ± 3.79
Duration, h	11	11	11	11
Preroughened	Yes	Yes	No	Yes
Altitude, cm	31	32	32	32

initial measured load. The duration of each exposure, and the z position of the fixture above the chamber floor (altitude in Table 4) is given. Loads between 6 and 30 MPa were investigated because of the range of stresses expected in HETs and also because of the failure loads of two sacrificial $3 \times 1 \times 0.25$ in. fused-silica samples. Two samples failed at 28.9 ± 1.2 MPa and 29.4 ± 1.2 MPa.

A. Amplification Functions

Exposures 1, 2, and 4 yielded consistent results for the amplification functions. Preroughening of the sample surfaces ensured that enough initial surface structure was present to avoid problems with source dirt and uneven operation encountered in previous iterations of the experiment. Exposure 1 produced erosion depths of 30–50 μm on the sample pair, as measured from the step height from the area shadowed by the clamp to the exposed area of the samples. Exposure 2 produced 20–40 μm erosion depths. Exposure 4 produced 30–40 μm erosion depths.

Figure 12 shows the amplification functions derived from the line scans for exposures 1, 2, and 4. Each amplification function is a comparison between averages of 50 initial and final Fourier transformed line scans. The standard deviation of the mean is approximately the width of noise in the data. The amplification functions show a range of growth in the surface features, for wavelengths greater than approximately 0.1 mm (wave numbers less than 10 mm^{-1}). The pattern is consistent between the sample pairs. Between each exposure, there is a difference in Ψ [0.05 (nondimensional) or less], probably linked to the difference in the erosion depth. No difference is apparent in the evolution of the control compared to the loaded samples for any of the three exposures.

To better show the closeness of the match between the amplification functions, Fig. 13 shows seven-point spatial frequency averages of the data to reduce the noise. The amplification functions for a sample pair (SA10 and SA6, for example) are almost exactly coincident. Between the series, there is a variation of between 0.1 and 0.05 in the value of Ψ.

These results show that a growth process is operating on the initial preroughened amorphous fused-silica samples. The final surface roughness Fourier components are an amplified linear function of the initial surface Fourier roughness components. The observed process of erosion does not appear to be a function of the applied thermomechanical loading in these amplification function diagrams, for up to 25.0 MPa of compression.

B. Surface Crystallography

X-ray diffraction crystallography (XRD) was conducted for four of the samples. The XRD was conducted on samples SA4 and SA7 after plasma exposure and on samples SA6 and SA10 before exposure. Sample SA6 was preroughened, and sample SA10 was as manufactured (smooth) during the crystallography. XRD revealed the presence of any crystalline grains in a material as a series of sharp peaks much greater than the noise floor. Figure 14 shows the XRD traces on the exposed surface of each sample. All traces, for both exposed and unexposed samples, smooth and preroughened, show the same amorphous curve without significant peaks. This demonstrates that no crystalline grains were present in or on the surface. The fused-silica material was amorphous before exposure, and after exposure, no crystallization took place.

The XRD analysis confirmed that the material was amorphous and remained amorphous after exposure to the plasma. The temperatures reached by the samples during exposure were not more than 500°C, which is 200–300°C greater than the temperatures reached by the test fixture during the exposures. This information is from additional testing with thermocouples attached to the sample as well as the test fixture. The sample temperatures were well below the annealing temperature of SiO_2, which is 1215°C [27].

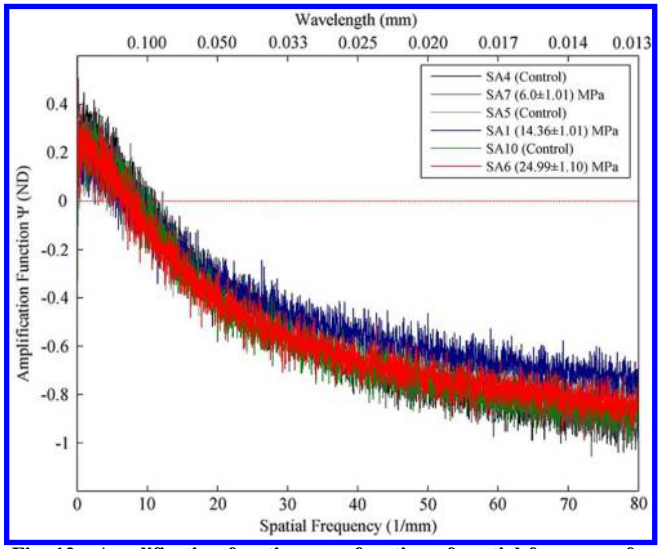

Fig. 12 Amplification function as a function of spatial frequency for exposures 1, 2, and 4.

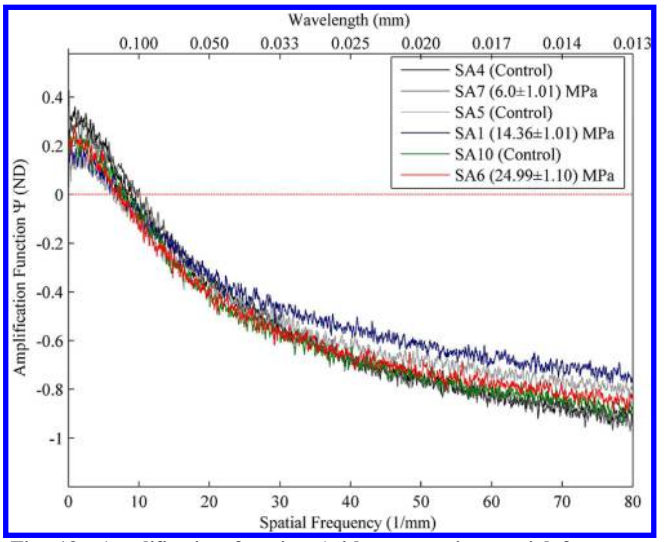

Fig. 13 Amplification function (with seven-point spatial frequency average) as a function of spatial frequency.

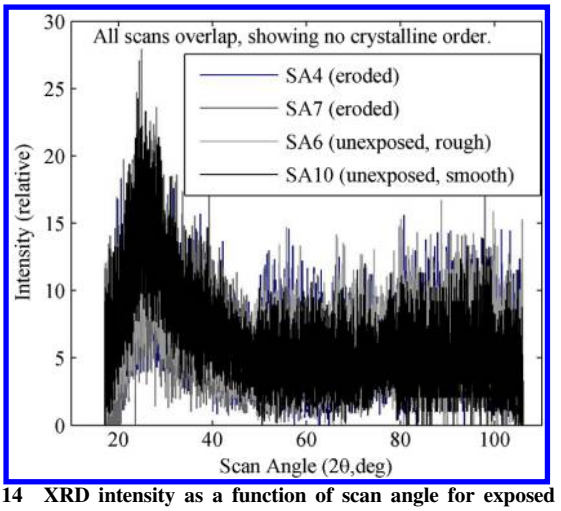

Fig. 14 XRD intensity as a function of scan angle for exposed and unexposed samples.

C. Pre- and Posttest Surface Microscopy

Microscopy was conducted to produce three-dimensional surface height maps and images of the features developed by the plasma erosion process. Figure 15 shows the development of a cellular pattern produced by the erosion process acting on the preroughened sample surfaces. Figure 15 shows a height profile (a and c) taken using the Olympus LEXT laser microscope and a laser profile image (b and d). The images were taken near the center of the sample, at the

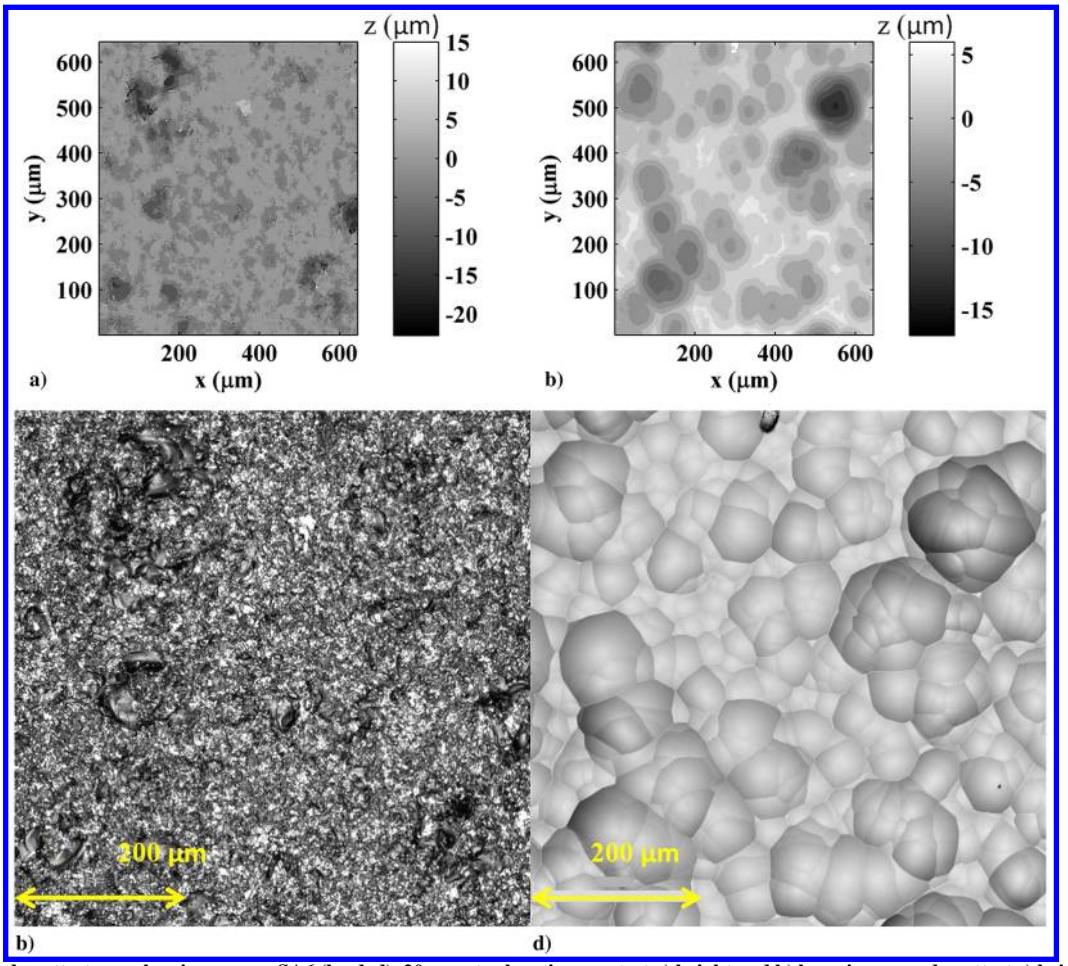

Fig. 15 Pre- and posttest sample microscopy: SA6 (loaded), 20x, center location: pretest a) height and b) laser image and posttest c) height and d) laser image.

same locations before and afterward. The reacquisition of the same location was done by measuring from the lower left corner of each sample with the motion stage of the microscope.

On all the preroughened samples, a cell pattern developed from the random white-noise initial roughness pattern. Figure 16 shows some representative line-scan profiles that reveal that each of these cells was a smooth, mostly parabolic depression, bounded by sharp-edged cusps. The surface had the overall appearance of a plane divided into Voronoi-like cells. Each cell was a cup (concave), not a bubble (convex). The distance between pre- and posttest line scans in Fig. 16 is not to scale; it is intended to show each line scan side by side.

For exposure 3, two samples, SA8 and SA9, were exposed under the same load conditions as exposure 2 (14.9 MPa). The surfaces of these samples were left smooth ($\pm.05$ μm), as manufactured, except for a small area of sample SA9. This area was scored with the tip of a 1/16 in. fine-pointed screwdriver to create a limited region where initial surface roughness was present.

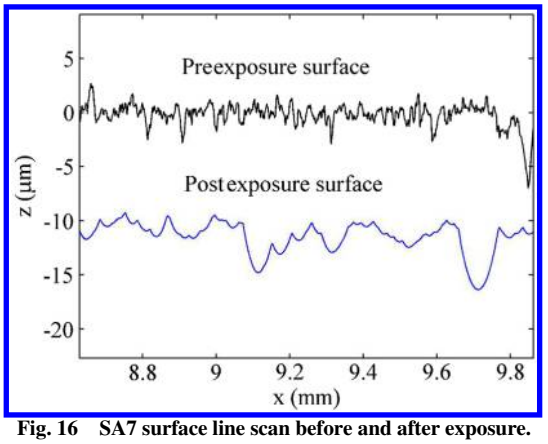

Fig. 16 SA7 surface line scan before and after exposure.

Figure 17 shows the comparison of the scored region before and after exposure. Postexposure, the unmarked regions of the smooth samples remained smooth in the microscope images taken with the LEXT. No apparent surface features resulting from a growth process appeared to be present. However, the marked region shows the beginning of the same cell structure seen on the preroughened samples.

This test demonstrates that the surfaces developed according to a growth or amplification process. In the absence of initial surface roughness, the surfaces remained flat. If there was initial surface roughness, the cell pattern developed. The growth process that was observed for fused silica seemed to depend only on the initial surface geometry. In the next section, the question of what caused the development of the observed cell pattern is investigated. A plausible mechanism for the development and growth of the cells is provided in the discussion section.

IV. Discussion

The stressed erosion experiment is intended to find dependence of the process of plasma erosion on the presence of mechanical stress in materials. Instabilities in the surface driven by the presence of mechanical strain energy could potentially lead to the growth of regular features such as the anomalous erosion ridges. For amorphous fused silica, for stresses of up to 25 MPa, no dependence of the erosion process on applied mechanical stress was seen. However, a cell pattern was observed to grow from initial seed surface roughness. Section IV.A describes a model that explains the development of the observed cell pattern. Section IV.B discusses the effects of working

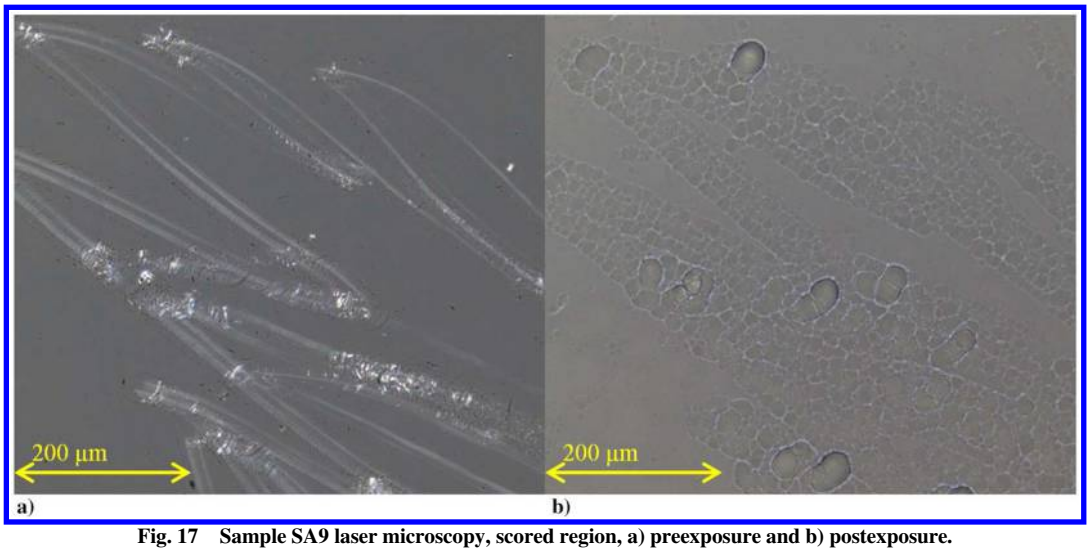

Fig. 17 Sample SA9 laser microscopy, scored region, a) preexposure and b) postexposure.

gas and sample temperatures on the results of the experiment. Section IV.C discusses the degree of similarity between the loaded and control samples and the time scale of stress-dependent phenomena that the experiment eliminates as a possibility.

A. Mechanism Explaining Cell Pattern Development in Fused Silica

The simplest hypothesis that plausibly explains the growth of the cell patterns is that it is the result of the angle dependence of the sputtering yield of the material. Under normal ion bombardment, the angle that the surface makes to the incoming ions modifies the sputtering yield. In sputtering yield theory and experiment, the yield tends to peak at ion incidences of 50–80 deg from the surface normal of the target. In a semi-infinite medium, there will be an angle at which the repulsive action of the surface atoms prevents the ions from penetrating into the target (and hence a falloff in yield). At lower angles, though, the size of the region of energized target atoms that lies close enough to the surface to allow atoms to escape the target scales as $1/\cos(\theta)$, with θ being the ion angle relative to the surface normal. If the ion mass is greater than the atomic mass in the target, as is the case for Ar and Xe with a SiO_2 target, then $1/\cos(\theta)$ is a good model. If the masses are more nearly equal, the angle dependence scales as $1/\cos(\theta)^{5/3}$ [29,30].

For the following analysis, a curve fit, of the modified Yamamura form, is made to empirical angle-dependent yield data collected by Yalin et al. [6] for Xe sputtering of fused quartz. The form of the model is given in Eq. (15), while the coefficients to the model are given in Table 5. The angle dependence of the yield is shown in Fig. 18, showing that a third-degree polynomial fit to the data peaks at 55 deg ion incidence to the surface normal,

$$Y(E,\theta) = f(\theta)g(E) = (B_0 + B_1\theta + B_2\theta^2 + B_3\theta^3)k\sqrt{E}\left(1 - \sqrt{\frac{E_{\text{th}}}{E}}\right)^{2.5} \quad (15)$$

Table 5 Yield model fitting coefficients

Variable	Value
k, $\text{mm}^3/\text{C}\cdot\text{eV}^{0.5}$	5.0×10^{-3}
E_{th}, eV	15.0
B_0	1
B_1, 1/deg	0
B_2, $1/\text{deg}^2$	1.11×10^{-3}
B_3, $1/\text{deg}^3$	-1.37×10^{-5}

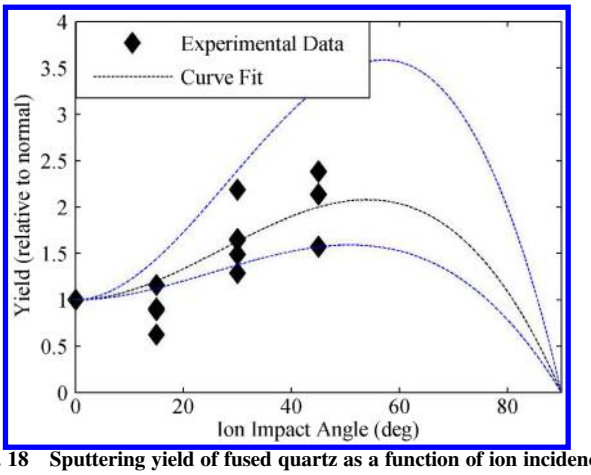

Fig. 18 Sputtering yield of fused quartz as a function of ion incidence angle. Data from [6]. Curve fits for best fit, minimum, and maximum angle dependence.

Townsend [30] noted that, due to the higher sputtering yield of surfaces at an angle to an ion beam, certain initial surface profiles, such as spheres or sinusoidal surfaces, would develop, over time, into cones or cusps as erosion proceeds [30]. A one-dimensional simulation of the evolution of a surface profile by atomic sputtering that demonstrates this behavior is constructed. The simulation calculates the rate of erosion at each point along a surface profile as a function of the surface normal of the neighboring area elements. Using the surface normal of two neighboring elements allows the nodes to act as a hinge and allows the simulation to handle sharp cusps without numerical instability. The simulation evolves the surface profile in time, producing eroded surface profiles from uneroded surface profiles. Time steps of 5 s are used to simulate the evolution of surface profiles with a 0.4 nm horizontal spacing between nodes. Ion current densities of 10 mA/cm^2 and ion energies of 100 eV are used, similar to conditions in the IAD chamber experiment. Figure 19 shows relative error as a function of time step between simulations. This demonstrates that the simulation is well converged for 5 s time steps. The reference solution is one run at 2.5 s time steps, to which the other solutions are compared.

Figure 20 shows the evolution of a sinusoidal profile, showing the development of cusp shapes. The sloped edges erode faster than the land at the top and bottom of the profile, leading to a widening of the base and narrowing of the peak of the profile.

A 500 μm section is taken from the pre- and posttest line scans from sample SA6. A simulation of the erosion of the top surface is propagated forward in time for 11 h. At erosion depths similar to the ones reached during the 11 h experimental exposure, a profile with

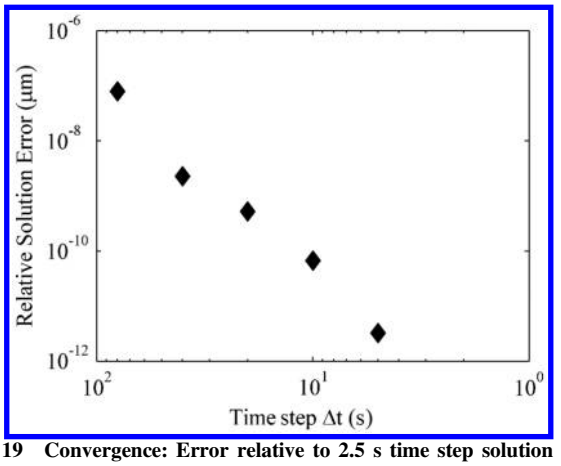

Fig. 19 Convergence: Error relative to 2.5 s time step solution as a function of time step.

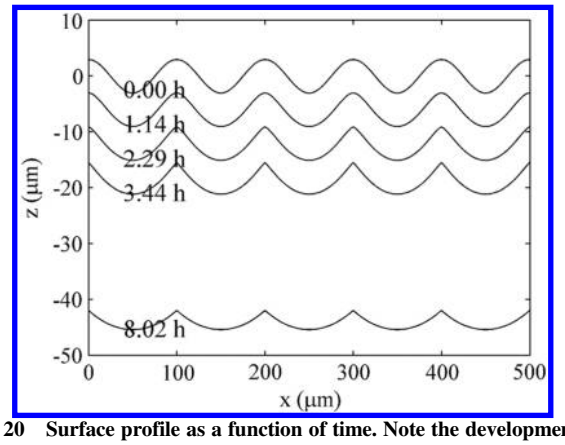

Fig. 20 Surface profile as a function of time. Note the development of cusps from initial sinusoidal features.

features similar to the experimental posttest surface is observed. Figure 21 shows the pre- and posttest line scans in blue, and several time steps of the simulated evolution of the top profile in black. The actual surface is two dimensional, and so there is an extra dimension for the profile to be off normal to the ion beam, but even with a one-dimensional simulation, features of a similar depth and profile to the posttest surface develop.

Because of the similarity in features between the simulated and measured surface profiles, it is believed that pure local atomic sputtering is sufficient to explain the development of the cusps and cellular pattern on the posttest surfaces from the initial surface profile. This mechanism is purely local, and therefore the only length scales present in the problem physics are the length scales involved in the initial surface roughness and the average depth of the erosion.

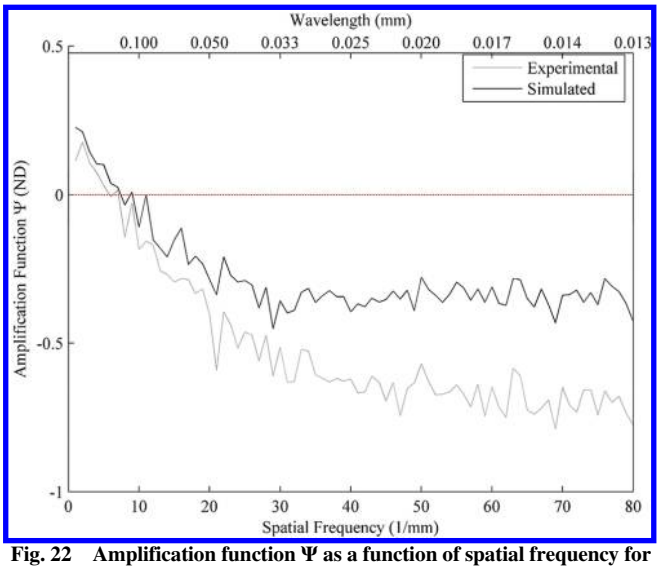

Fig. 22 Amplification function Ψ as a function of spatial frequency for experimental and simulated profiles.

Fifty 1-mm-long samples of the surface line scans are propagated to the average erosion depth using the model, and Fourier statistics, similar to those measured experimentally, are derived. Figure 22 shows a comparison of the amplification function for the experimental and modeled profiles for sample SA6. These amplification functions have less spatial frequency resolution than the ones shown in Fig. 13 due to the smaller length of the simulated domain but show the same general trend. Both the simulated and experimental amplification profiles show growth of features with longer wavelength than 0.1 mm and damping of smaller wavelengths. The amplification statistics agree well until approximately 30 mm^{-1}; after that, the simulation shows less damping of higher-frequency features than the physical process. This might point to the existence of a smaller-order diffusive process not captured in the model. Arguably, high spatial frequency information, due to the smaller order-of-magnitude initial and final amplitudes, is noisier and less important in defining the pre- and posttest surfaces. The agreement at spatial frequencies below 30 mm^{-1} corresponds to the qualitative similarity between the modeled and experimental posttest surfaces.

It may also be the case that the pattern will not persist for arbitrary erosion depths; the top and bottom of the profile, with the exception of any cusps that develop, are normal to the ion beam and therefore must erode at the same rate. The cusps erode faster than this and may vanish given enough time. Therefore, in the absence of surface features inclined at more than 55 deg to the normal, the range of the profile predicted by this mechanism is bounded above by the initial profile range. The average curvature and profile depth of the modeled sin waves show this behavior; after the development of the cusps at 20 μm depth, the average curvature peaks. The depth of the profile begins to decrease with further erosion. Figure 23 shows the envelope

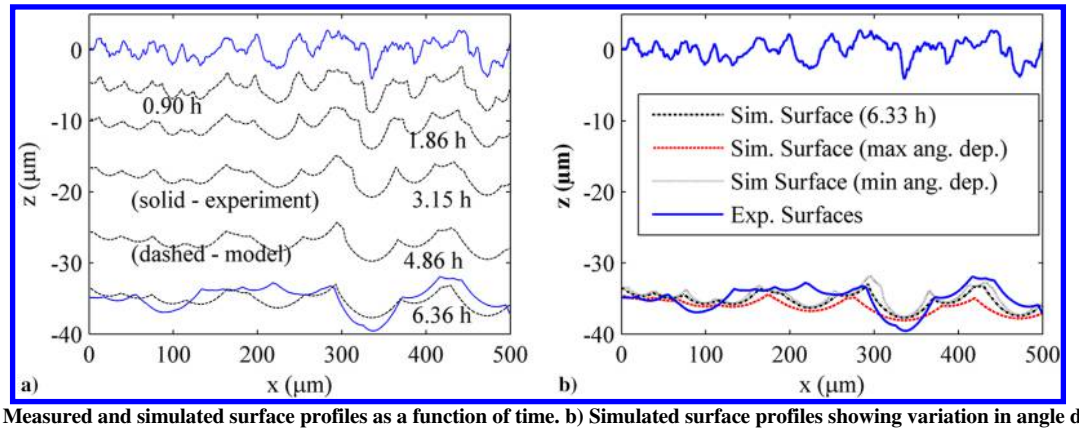

Fig. 21 a) Measured and simulated surface profiles as a function of time. b) Simulated surface profiles showing variation in angle dependence.

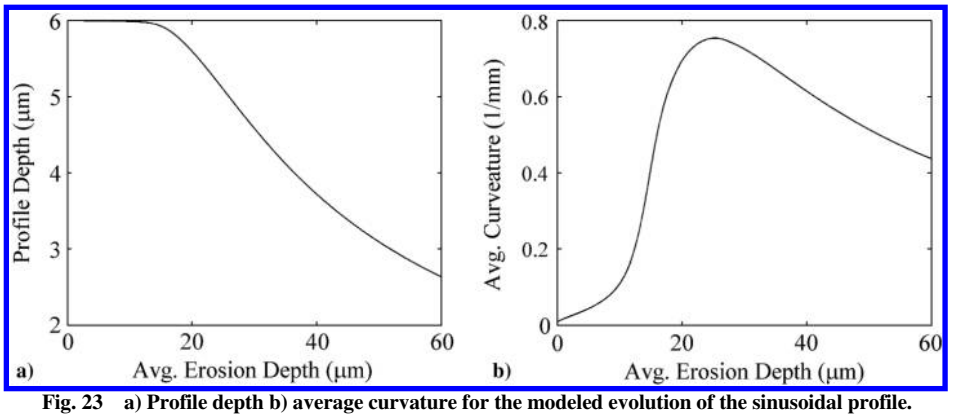

Fig. 23 a) Profile depth b) average curvature for the modeled evolution of the sinusoidal profile.

height and average curvature as a function of the average erosion depth for the sinusoidal profiles.

B. Effects of Ion Mass and Temperature

In the stressed erosion experiment, the equilibrium temperature that the clamp and samples attain is important primarily in how much relaxation is produced due to the thermal expansion of the clamp screw. Prior research on atomic sputtering by Sigmund [29] and Rosenberg and Wehner [35] states that the sputtering yield of a target material is insensitive to the material temperature. The stressed erosion experiment uses argon gas instead of xenon, which is commonly used in HETs. However, the sputtering yield for the energies of interest in HET physics (tens to hundreds of electron volts) is insensitive to ion mass with the exception of the lightest ions like helium. Experimental data analyzed by Sigmund shows that below 1 keV there is not a lot of difference between argon, krypton, and xenon sputtering yields of polycrystalline metals such as silver and copper. At high energies, above approximately 50 keV, the sputtering yield (atoms/ion) for xenon is a factor of 2 greater than the sputtering yield for argon. Rosenberg and Wehner investigate helium, krypton, and xenon sputtering of a wide variety of target materials at 100, 200, 300, and 600 eV ion energies. The sputtering yields for krypton and xenon are similar. This research suggests that using argon, or krypton, in place of xenon should not result in significant differences in the sputtering yield of the material at the energies important to HET physics and erosion. At most, there should be a factor of 2 difference for kiloelectron volt ion impact energies.

C. Time Constant Analysis of Potential Stress-Dependent Process and Surface Statistics

Long-duration HET life testing takes place over the course of thousands of hours. This experiment is limited to exposures shorter than 12 h because of the length of time in which the plasma source will operate with a uniform discharge. However, the accuracy and spatial frequency resolution of the Tencor surface profiles allow statements to be made that rule out the presence of an autonomous stress-dependent growth process that is faster than a given time constant.

If the anomalous erosion ridges result from a process driving the growth of initial surface features into a final ridge pattern, then this implies an upper bound on the time constant of the growth process. The growth process must be capable of growing features from the micrometer scale of initial surface roughness to the millimeter scale of the depth of the erosion ridges over the course of long-duration life testing or long-duration operation of the thruster. Equation (16) shows how a given wave component would grow autonomously time. In this equation, a is the amplitude of a surface wave or variation to the average profile, t is the elapsed exposure time, and τ is the time constant of the growth process.

$$a(t;\omega) = a(0;\omega)\exp[t/\tau(\omega)] \tag{16}$$

Garner's life testing of the SPT-100 includes figures that show the presence of the anomalous ridges after 1795 h of operating the thruster [12], implying a maximum time constant of growth of about 260 h at most. The work with the PPS-1350G of Mazouffre et al. [17] shows the presence of the ridges after a 3500 h life test, implying a maximum 500 h time constant [17].

The sensitivity and spatial frequency resolution of the Tencor profilometry allows a very accurate measurement of a lower bound for the time constant of a hypothetically stress-dependent growth process acting on the initial surfaces of the samples. A Euclidean functional distance between the amplification functions for the stressed and control sample can be defined according to Eq. (17). This provides the average rms distance between the amplification functions,

$$< \Delta\Psi >= \sqrt{\frac{\int_0^{\omega_f} |\Psi_1(\omega) - \Psi_2(\omega)|^2 \, \mathrm{d}\omega}{|\omega_f - 0|}} \tag{17}$$

Using this functional to measure the difference in amplification between the loaded and control sample of exposure 4, a value of 0.018 is found for $< \Delta\Psi >$. In this calculation, a cutoff of 40 mm^{-1} and 100 point spatial frequency averaging were used. This implies that if a stress-dependent growth process were present it must have a time constant of more than 280 h, or a stronger difference between the loaded and control amplification functions would be observed. Equation (18) relates $< \Delta\Psi >$ to the time constant of the growth process. This implies that for the fused-silica erosion any stress-dependent growth process must grow more slowly (280 h) than the slowest process that could explain the erosion ridges in the SPT-100 (260 h). In addition, the evolution of the fused-silica surface is dominated by a faster process, insensitive to applied stress, with a time constant of only 26 h.

$$\tau = \frac{t}{\ln(10) < \Delta\Psi >} \tag{18}$$

V. Conclusions

Hall effect thrusters (HETs) in operation attain high temperatures and have significant thermomechanical stresses within the discharge chamber material. In addition, the discharge channel presents unexplained erosion features. To investigate whether or not thermomechanical stress may alter the manner in which material erodes due to atomic sputtering, an experiment was designed to place material samples under a mechanical load. Amorphous fused-silica samples, loaded to 6.00 ± 1.01, 14.36 ± 1.01, and 24.99 ± 1.10 MPa, respectively, exhibited no difference in the erosion patterns on the surface of loaded vs unloaded samples. A cell pattern was developed in preroughened amorphous fused silica. A mechanism describing the development of the cusped cell pattern as resulting from the ion incidence angle dependence of the local atomic sputtering yield was proposed. Modeling of this mechanism successfully reproduced observed posttest surface characteristics and the Fourier statistics observed experimentally. The length scales governing the horizontal scale of the cell pattern in the

fused-silica surface were the erosion depth and the length scale of the initial surface roughness.

The development of surface features during the plasma erosion of a simple, isotropic, amorphous material was not measurably a function of the applied mechanical load, up to stresses of 25.0 MPa. However, it was found that complex surface features can develop from initial surface roughness due to the angle dependence of the sputtering yield.

Acknowledgments

This work was funded by a National Defense Scientific and Engineering Graduate fellowship and by the Air Force Office of Scientific Research under grant number FA9550-11-1-0160. The authors would like to thank the American Society for Engineering Education and Air Force Office of Scientific Research for supporting this research. In addition, the authors would also like to thank Thomas Burton and Gregory B. Thompson of the University of Alabama for help in conducting x-ray diffraction crystallography. The authors would like to thank Jud Ready and Brent Wagner of Georgia Tech Research Institute for the use of their chamber and plasma source.

References

[1] Dudeck, M., Doveil, F., Arcis, N., and Zurbach, S., "Plasma Propulsion for Geostationary Satellites and Interplanetary Spacecraft," *Romanian Journal of Physics*, Vol. 56, Jan. 2011, pp. 3–14. doi:10.1088/1757-899x/29/1/012010

[2] Clauss, C., Day, M., Kim, V., Kondakov, Y., and Randolph, T., "Preliminary Study of Possibility to Ensure Large Enough Lifetime of SPT Operating Under Increased Powers," *Proceedings of the 33rd Joint Propulsion Conference and Exhibit, Joint Propulsion Conferences*, AIAA Paper 1997-2789, 1997. doi:10.2514/6.1997-2789

[3] Goebel, D. M., and Katz, I., *Fundamentals of Electric Propulsion: Ion and Hall Thrusters*, Vol. 1, Wiley, Hoboken NJ, 2008, pp. 325–389. doi:10.1002/9780470436448

[4] Garnier, Y., Viel, V., Roussel, J. F., Pagnon, D., Mange, L., and Touzeau, M., "Investigation of Xenon Ion Sputtering of One Ceramic Material Used in SPT Discharge Chamber," *Proceedings of the 26th International Electric Propulsion Conference*, Electric Rocket Propulsion Soc., Kitakyushu, Japan, Oct. 1999, pp. 512–517.

[5] Garnier, Y., Viel, V., Roussel, J.-F., and Bernard, J., "Low-Energy Xenon Ion Sputtering of Ceramics Investigated for Stationary Plasma Thrusters," *Journal of Vacuum Science and Technology*, Vol. 17, No. 6, 1999, pp. 3246–3254. doi:10.1116/1.582050

[6] Yalin, A. P., Rubin, B., Domingue, S. R., Glueckert, Z., and Williams, J. D., "Differential Sputter Yields of Boron Nitride, Quartz, and Kapton Due to Low Energy Xe+ Bombardment," AIAA Paper 2007-5314, 2007. doi:10.2514/6.2007-5314

[7] Peterson, P. Y., Manzella, D., and Jacobson, D., "Investigation of the Erosion Characteristics of a Laboratory Hall Thruster," *Proceedings of the 39th AIAA/ASME/SAE/ASEE Joint Propulsion Conference and Exhibit, Joint Propulsion Conferences*, AIAA Paper 2003-5005, 2003. doi:10.2514/6.2003-5005

[8] Fife, J. M., "Hybrid-PIC Modeling and Electrostatic Probe Survey of Hall Thrusters," Massachusetts Inst. of Technology, 1998.

[9] Gamero-Castano, M., and Katz, I., "Estimation of Hall Thruster Erosion Using HPHall," *Proceedings of the 29th International Electric Propulsion Conference*, Electric Propulsion Rocket Soc. Paper 2005-303, Princeton Univ., Princeton, NJ, 2005.

[10] Hofer, R. R., Mikellides, I. G., Katz, I., and Goebel, D. M., "BPT-4000 Hall Thruster Discharge Chamber Erosion Model Comparison with Qualification Life Test Data," *Proceedings of the 30th International Electric Propulsion Conference*, Electric Propulsion Rocket Soc., Florence, Italy, 2007, pp. 17–20.

[11] De Grys, K. H., Mathers, A., Welander, B., and Khayms, V., "Demonstration of 10,400 Hours of Operation on 4.5 kW Qualification Model Hall Thruster," *Proceedings of the 46th AIAA/ASME/SAE/ASEE Joint Propulsion Conference and Exhibit, Joint Propulsion Conferences*, AIAA Paper 2010-6698, 2010. doi:10.2514/6.2010-6698

[12] Garner, C. E., Brophy, J., and Polk, J., "A 5,730-Hr Cyclic Endurance Test of the SPT-100," *Proceedings of the 31st Joint Propulsion Conference and Exhibit, Joint Propulsion Conferences*, AIAA Paper 1995-2667, July 1995. doi:10.2514/6.1995-2667

[13] Zurbach, S., Duchemin, O. B., Vial, V., Marchandise, F., Cornu, N., and Arcis, N., "Qualification of the PPS-1350 Hall Thruster at 2.5 kW," *Proceedings of the 49th AIAA/ASME/SAE/ASEE Joint Propulsion Conference, Joint Propulsion Conferences*, AIAA Paper 2013-4113, July 2013. doi:10.2514/6.2013-4113

[14] Morozov, A. I., "The Conceptual Development of Stationary Plasma Thrusters," *Plasma Physics Reports*, Vol. 29, No. 3, 2003, pp. 235–250. doi:10.1134/1.1561119

[15] De Grys, K., Meckel, N., Callis, G., Greisen, D., Hoskins, A., King, D., Wilson, F., Werthman, L., and Khayms, V., "Development and Testing of a 4500 Watt Flight Type Hall Thruster and Cathode," *Proceedings of the 27th International Electric Propulsion Conference*, Electric Propulsion Rocket Soc., Pasadena, CA, Oct. 2001; also IEPC Paper 2011-011, Oct. 2001.

[16] Morozov, A. I., and Savelyev, V. V., "The Electron Dynamics in SPT-Channel and the Problem of Anomalous Erosion," *Proceedings of the 24th International Electric Propulsion Conference*, Electric Propulsion Rocket Soc., Moscow, Russia, 1996, pp. 331–338.

[17] Mazouffre, S., "Plasma Induced Erosion Phenomena in a Hall Thruster," *Proceedings of the Recent Advances in Space Technologies*, Inst. of Electrical and Electronics Engineers, Istanbul, Turkey, 2003, pp. 69–74. doi:10.1109/RAST.2003.1303393

[18] Schinder, A., Walker, M. L. R., and Rimoli, J. J., "3D Model for Erosion of a Hall Effect Thruster Discharge Channel Wall," *Journal of Propulsion and Power*, Vol. 30, No. 5, 2014, pp. 1373–1382. doi:10.2514/1.B35098

[19] Suo, Z., "Motions of Microscopic Surfaces in Materials," *Advances in Applied Mechanics*, Vol. 33, Academic Press, New York, 1997, pp. 193–294. doi:10.1016/s0065-2156(08)70387-9

[20] Asaro, R. J., and Tiller, W. A., "Interface Morphology Development During Stress Corrosion Cracking: Part I. Via Surface Diffusion," *Metallurgical Transactions*, Vol. 3, No. 7, 1972, pp. 1789–1796. doi:10.1007/BF02642562

[21] Kim, K.-S., Hurtado, J. A., and Tan, H., "Evolution of a Surface-Roughness Spectrum Caused by Stress in Nanometer-Scale Chemical Etching," *Physical Review Letters*, Vol. 83, No. 19, 1999, pp. 3872–3875. doi:10.1103/PhysRevLett.83.3872

[22] Mazouffre, S., Luna, J. P., Gawron, D., Dudeck, M., and Echegut, P., "An Infrared Thermography Study on the Thermal Load Experienced by a High Power Hall Thruster," *Proceedings of the 29th International Electric Propulsion Conference*, IEPC Paper 2005-63, Electric Propulsion Rocket Soc., Princeton, NJ, 2005. doi:10.1109/tdmr.2013.2279253

[23] Martinez, R. A., Dao, H., and Walker, M. L. R., "Power Deposition into the Discharge Channel of a Hall Effect Thruster," *Journal of Propulsion and Power*, Vol. 30, No. 1, 2014, pp. 209–220. doi:10.2514/1.B34897

[24] Katz, I., Mikellides, I. G., and Hofer, R. R., "Channel Wall Plasma Thermal Loads in Hall Thrusters with Magnetic Shielding," *47th AIAA/ASME/SAE/ASEE Joint Propulsion Conference and Exhibit*, Vol. 608, AIAA Paper 2011-6082, 2011. doi:10.2514/6.2011-6082

[25] Hobbs, G. D., and Wesson, J. A., "Heat Flow Through a Langmuir Sheath in Presence of Electron Emission," *Plasma Physics*, Vol. 9, No. 1, 1967, pp. 85–87. doi:10.1088/0032-1028/9/1/410

[26] "COMBAT Boron Nitride Solids Product Datasheet," St. Gobain Ceramic Materials, [online manufacturer's property sheet], 2011, http://www.bn.saint-gobain.com/combat-bn-solids.aspx [retrieved 5 April 2016].

[27] "Properties of Fused Quartz," Technical Glass Products [online manufacturer's property sheet], http://www.technicalglass.com/technical_properties.html [retrieved 7 Dec. 2014].

[28] *High-Temperature Characteristics of Stainless Steels*, Designer's Handbook Series, No. 9004, American Iron and Steel Inst., Jan. 1979, p. 17.

[29] Sigmund, P., "Theory of Sputtering. I. Sputtering Yield of Amorphous and Polycrystalline Targets," *Physical Review*, Vol. 184, No. 2, 1969, pp. 383–416. doi:10.1103/PhysRev.184.383

[30] Townsend, P., Kelley, J., and Hartley, N., "Chapter 6: Sputtering," *Ion Implantation, Sputtering and Their Applications*, Academic Press, New York, 1976, pp. 111–147.

[31] Michels, W. C., and Wilford, S., "The Physical Properties of Titanium. I. Emissivity and Resistivity of the Commercial Metal," *Journal of Applied Physics*, Vol. 20, No. 12, 1949, pp. 1223–1226. doi:10.1063/1.1698312

[32] Cairns, J. H., "Apparatus for Investigating Total Hemispherical Emissivity," *Journal of Scientific Instruments*, Vol. 37, No. 3, 1960, pp. 84–87. doi:10.1088/0950-7671/37/3/304

[33] Walker, M., Hofer, R., and Gallimore, A., "The Effects of Nude Faraday Probe Design and Vacuum Facility Backpressure on the Measured Ion Current Density Profile of Hall Thruster Plumes," *Proceedings of the 38th AIAA/ASME/SAE/ASEE Joint Propulsion Conference & Exhibit, Joint Propulsion Conferences*, AIAA Paper 2002-4253, July 2002. doi:10.2514/6.2002-4253

[34] Williams, L., "Ion Acceleration Mechanisms of Helicon Thrusters," Ph. D. Dissertation, Georgia Inst. of Technology, Atlanta, GA, 2013.

[35] Rosenberg, D., and Wehner, G. K., "Sputtering Yields for Low Energy He^{+-}, Kr^{+-}, and Xe^{+-} Ion Bombardment," *Journal of Applied Physics*, Vol. 33, No. 5, 1962, pp. 1842–1845.

B. King
Associate Editor